

An RGB-Achromatic Aplanatic Metalens

Junhao Li, Wenwei Liu, Haofei Xu, Zhaorui Huang, Jian Wang, Jing Wen, Jia Yang, Jianguo Guan, Shuming Wang, Andrea Alù, Zhang-Kai Zhou,* Shuqi Chen,* and Lin Chen*

Optical metalenses offer a compact approach for the development of nanoscale optical devices with various imaging functionalities. Realizing high-quality images using metalenses with large numerical aperture (NA) requires eliminating unwanted optical aberrations. Existing strategies have largely focused only on correcting chromatic aberrations, and a metalens capable of simultaneously correcting chromatic and spherical aberrations has not yet been developed. Here, this issue is addressed by realizing an aplanatic phase profile for a red–green–blue (RGB) achromatic metalens, thereby demonstrating an RGB-achromatic aplanatic metalens. This device consists of crystalline silicon nanostructures and it enables RGB-achromatic aplanatic focusing with an NA of 0.635. The focal length of metalens remains unchanged at the three RGB wavelengths, whereas the associated focal spots are significantly smaller than those of an RGB-achromatic metalens with spherical aberrations. An enhanced RGB imaging resolution is demonstrated, offering exciting opportunities to power up various imaging and display applications using flat metalenses.

1. Introduction

Optical lenses are widely used in imaging tools such as cameras, binoculars, and telescopes. The numerical aperture (NA) of an optical lens is a key figure of merit for its imaging operation that is important both for achieving high imaging resolution and for maximizing light collection. The main challenge in the lens design is arranging a phase profile that achieves a high NA while eliminating optical aberrations, such as chromatic and spherical aberrations. A single high-NA glass lens cannot simultaneously correct chromatic and monochromatic aberrations, which makes it necessary to precisely align several lenses to remove optical aberrations in traditional imaging systems. However, the resulting systems are bulky, expensive, and

J. Li, Z. Huang, J. Wang, L. Chen
Wuhan National Laboratory for Optoelectronics and School of Optical and Electronic Information
Huazhong University of Science and Technology
Wuhan 430074, China
E-mail: chen.lin@mail.hust.edu.cn

W. Liu, S. Chen
The MOE Key Laboratory of Weak Light Nonlinear Photonics, School of Physics and TEDA Institute of Applied Physics
Nankai University
Tianjin 300071, China
E-mail: schen@nankai.edu.cn

H. Xu, Z.-K. Zhou
State Key Laboratory of Optoelectronic Materials and Technologies, School of Physics
Sun Yat-sen University
Guangzhou 510275, China
E-mail: zhouzhk@mail.sysu.edu.cn

J. Wen
Engineering Research Center of Optical Instrument and Systems, Ministry of Education and Shanghai Key Lab of Modern Optical System
University of Shanghai for Science and Technology
Shanghai 200093, China

J. Yang
R&D Department
China Academy of Launch Vehicle Technology
Beijing 100076, China

J. Guan
State Key Laboratory of Advanced Technology for Materials Synthesis and Processing
Wuhan University of Technology
Wuhan 430074, China

S. Wang
National Laboratory of Solid State Microstructures
School of Physics
Nanjing University
Nanjing 210093, China

A. Alù
Photonics Initiative
Advanced Science Research Center
City University of New York
New York, NY 10031, USA

A. Alù
Physics Program
Graduate Center
City University of New York
New York, NY 10016, USA

 The ORCID identification number(s) for the author(s) of this article can be found under <https://doi.org/10.1002/lpor.202300729>

DOI: 10.1002/lpor.202300729

complex to operate, significantly limiting their application in portable and wearable devices. Metasurfaces have provided a new platform for the extreme control of light waves; thus, they are promising for the development of various ultrathin optical elements for applications such as lenses, holography systems, polarimeters, polarization elements, retroreflectors, and optical imaging encoding.^[1–14]

As one of the most important classes of metasurfaces, metalenses hold great promise for color imaging and display applications but face significant challenges for practical applications. A monochromatic metalens can achieve a high NA, with imaging performance comparable to state-of-the-art commercial objectives.^[15] However, arranging a phase profile that achieves a high NA metalens while eliminating other optical aberrations is challenging,^[2,15,16] and most designs are limited to a single wavelength or narrow wavelength range, limiting applications for full-color imaging. Considerable attention has recently been paid to the realization of achromatic metalenses over a wide continuous wavelength range by engineering the waveguide modes (or resonant modes) of meta-atoms to compensate for the natural dispersion that induces chromatic aberrations.^[17–21] The associated NA and working bandwidth are restricted by the limited group delay achievable with meta-atoms, and the reported achromatic metalenses spanning the entire visible region suffer from a limited NA. In parallel with these advances, several studies have been devoted to multiwavelength achromatic metalenses that can eliminate chromatic aberrations at several discrete wavelengths.^[22–25]

In addition to chromatic aberration correction, minimizing monochromatic aberrations such as spherical aberrations is crucial for high-quality imaging with high NA metalenses.^[26–29] Spherical aberrations reduce focal strength which in turn undermines both image resolution and clarity. A single high NA metalens that can simultaneously correct chromatic and spherical aberrations is a significant challenge for metalens design and has not been achieved to date. In this study, we introduce an aplanatic phase profile for a red–green–blue (RGB) achromatic metalens, thereby achieving a high NA RGB-achromatic aplanatic metalens. Low-loss crystalline silicon (c-Si) nanostructures are used as building blocks to introduce the required phase profile at RGB wavelengths, ensuring a consistent focal spot for full-color images, and simultaneously correcting spherical aberrations. The focal length of our metalenses with an NA of 0.635 is preserved over a continuous wavelength region from 490 to 720 nm, while the associated focal spots are significantly smaller than those of an RGB-achromatic metalens with spherical aberrations. We demonstrate that the imaging performance of the proposed metalens is superior to the one of RGB-achromatic counterparts without spherical aberration correction.

2. Results

2.1. Design Principles

Generally, an RGB-achromatic metalens focuses incoming light waves of three RGB wavelengths at normal incidence (Figure 1a) imparting a hyperbolic phase profile:^[22,24,30]

$$\varphi_j(r) = \frac{2\pi}{\lambda_j} (F - \sqrt{F^2 + r^2}) \quad (1)$$

where λ_j is the light wavelength in free space ($j = 1, 2, 3$), F is the focal length, and $r = \sqrt{x^2 + y^2}$ is the distance from an arbitrary position (x, y) on the metalens to the center. The metalens has a diameter D , with associated NA = $\frac{D}{\sqrt{4F^2 + D^2}}$. However, such a metalens cannot accurately converge spherical waves emitted by a point source because spherical aberration is not corrected (Figure 1b). Here, we correct spherical aberrations at three RGB wavelengths for an RGB-achromatic metalens, as schematically shown in Figure 1c,d. According to the generalized Snell's law, the aplanatic phase profile is given by

$$\frac{d\varphi_j(r)}{dr} = -\frac{2\pi}{\lambda_j} (\sin \theta_3 + n_s \sin \theta_2) \quad (2)$$

where $\sin \theta_3 = \frac{r}{\sqrt{r^2 + s'^2}}$, $\sin \theta_2 = \frac{r_2}{\sqrt{r_2^2 + t_s^2}}$, s' is the image distance, n_s is the refractive index of the substrate, and t_s is the thickness of the substrate. According to Snell's law, we have $\sin \theta_1 = n_s \sin \theta_2$, where $\sin \theta_1 = \frac{r_1}{\sqrt{r_1^2 + l_1^2}}$, $\sin \theta_2 = \frac{r_2}{\sqrt{r_2^2 + l_2^2}}$, $r_1 + r_2 = r$, and $l_1 = s - t_s$ (s is the object distance), and r_2 is related to r with $\frac{r-r_2}{\sqrt{(r-r_2)^2 + (s-t_s)^2}} = \frac{n_s r_2}{\sqrt{r_2^2 + t_s^2}}$. Consequently, all variables in Equation (2) are related to r and, hence, $\varphi_j(r)$ can be retrieved once r is given. By applying this aplanatic phase profile to an RGB-achromatic metalens, we can achieve a high NA RGB-achromatic aplanatic metalens, in which the scattered light from a point source, associated with a broad incidence angle, can be focused onto one focal spot because of spherical aberration correction. This aplanatic metalens is expected to be superior to nonaplanatic metalenses in terms of imaging resolution and clarity.

The three operation wavelengths for our RGB metalens are set to $\lambda_1 = 490\text{nm}$, $\lambda_2 = 570\text{nm}$, and $\lambda_3 = 700\text{nm}$ to cover the RGB channels. The phase profiles for an RGB-achromatic aplanatic metalens and RGB-achromatic nonaplanatic metalens are tailored based on Equations (1) and (2), respectively, and are shown in Figure S1a–f in Note S1 (Supporting Information). The two metalenses have the same NA of 0.635, associated with $s = 700 \mu\text{m}$, $s' = 1000 \mu\text{m}$ and $F = 365 \mu\text{m}$. The SiO₂ substrate has a thickness $t_s = 400 \mu\text{m}$ and a refractive index of 1.455. Their phase difference is almost 0 in the paraxial region and gradually increases when deviating from the optical axis (Figure S1g–i in Note S1, Supporting Information). In other words, spherical aberrations are negligible for a metalens with a small NA but they cause nonnegligible problems to the imaging performance for a metalens with a large NA. To construct an RGB-achromatic aplanatic metalens, the meta-atoms should satisfy the desired phase distribution (Figure S1d–f, Supporting Information) at all three RGB wavelengths. The transmission phase can be folded into the 0–2 π range by adding an integer multiple of 2 π . Considering that the proposed metalens comprise numerous of meta-atoms, we should have sufficient degrees of freedom to realize an arbitrary combination of RGB phases, for example, covering the full 2 $\pi \times 2\pi \times 2\pi$ phase space. c-Si has been demonstrated to be a good platform for developing high-performance meta-devices in the visible region owing to its high refractive index and acceptable intrinsic loss.^[16,31–34] Here, meta-atoms belonging to the C₂-symmetry group are considered in the metalens design,

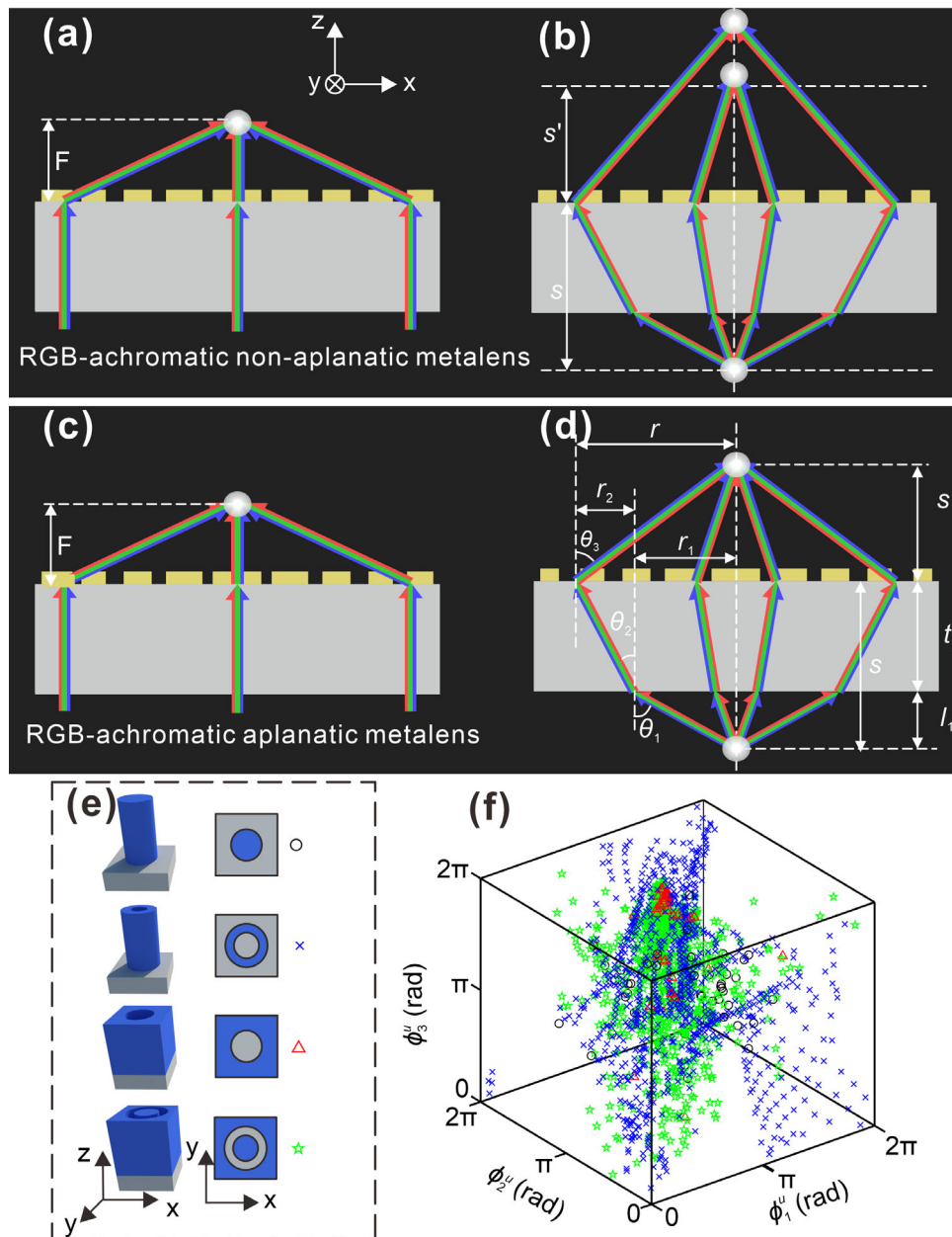


Figure 1. RGB-achromatic aplanatic metalens. a,b) Schematic of an RGB-achromatic nonaplanatic metalens under normal incidence of plane waves a) and spherical waves emitted by a point source b). c,d) Schematic of an RGB-achromatic nonaplanatic metalens under normal incidence of plane waves c) and spherical waves emitted by a point source d). e) Schematic of the unit cells. The left column is the schematic of the metasurface units, middle column is the top view, and right column is the corresponding mark in (f). f) Phases realized by the metasurface units (folded into $0-2\pi$). Each point corresponds to a specific metasurface unit. Each unit consists of a c-Si nanopillar with a thickness of 600 nm on a semi-infinite SiO_2 substrate. The permittivities of Si and SiO_2 are from the Palik model.^[37] All the simulations are conducted by FDTD using commercial software Lumerical FDTD Solutions.

consisting of a 600 nm-thick c-Si nanostructure on a SiO_2 substrate, and including four types of cross-sections (circle, ring, and their complementary graphics, Figure 1e). The lattice constants in the x - and y -directions are set at $p = 400\text{nm}$, close to the value predicted by Nyquist sampling theorem ($p < \frac{\lambda}{2NA}$) for the minimum operating wavelength,^[2] to minimize high-order diffraction phenomena. The 3D phase distribution of the c-Si meta-atom units clearly indicates that the provided transmission phase can completely fill the $2\pi \times 2\pi \times 2\pi$ phase space (Figure 1f).

In addition to the transmission phase, the focusing efficiencies of the three RGB channels are considered in the metalens design. Specifically, the weighted mean square error (WMSE) of complex transmission coefficients at an arbitrary point at a distance r from the metalens center is defined as

$$\text{WMSE}(r) = \sqrt{\sum_{j=1,2,3} a_j |t_j(r) - t_j^u|^2} \quad (3)$$

where $t_j(r) = \exp[i\varphi_j(r)]$ and $t_j^u = |t_j^u| \exp(i\varphi_j^u)$ are the theoretical complex transmission coefficient from Equation (3) and the complex transmission coefficient realized by the c-Si meta-atoms, respectively. φ_j^u is the phase shift caused by a c-Si meta-atom, and a_j represents the weighting coefficients used to adjust the focusing efficiency at different wavelengths. Considering that c-Si has the largest absorption loss at blue wavelengths, we used $a_1 = 0.5$ and $a_2 = a_3 = 0.25$ to increase the focusing efficiency at 490 nm in our design. The WMSE of the meta-atom at (x, y) ($r = \sqrt{x^2 + y^2}$) can be retrieved using by Equations (2) and (3), and the meta-atom with the minimum WMSE is selected (see Figure S2 in Note S1, Supporting Information for the optimized transmission phase and amplitude distributions imposed by c-Si meta-atoms).

Numerical simulations based on Fresnel diffraction are performed to evaluate the performance of the aplanatic metalens with an ideal phase distribution (see Figure S3 in Note S2, Supporting Information). Compared with the nonaplanatic metalens with the same NA, the focal spot of the aplanatic metalens has a larger peak intensity and a smaller full width at half-maximum (FWHM), even if the object to be imaged deviates laterally from the optical axis or longitudinally from the ideal object distance along the optical axis. We also apply Lumerical FDTD Solutions to further verify the performance of the aplanatic metalens. Because the computational simulation with a metalens of NA = 0.635 ($D = 600 \mu\text{m}$) is beyond the memory limit for this software, we used a metalens with a lower NA in the simulation. Under normal incidence, both the RGB-achromatic aplanatic and nonaplanatic metalenses achieve achromatic focusing at $\approx 490, 570,$ and 700 nm , while the nonaplanatic chromatic metalens shows a focusing effect only $\approx 570 \text{ nm}$ (see Figure S4 in Note S3, Supporting Information). Here, we have defined the focusing efficiency as the energy in three times the FWHM area divided by the energy of the incident light.^[35] The simulated focusing efficiencies for the RGB-achromatic aplanatic metalens are 1.58%, 2.99%, and 4.66% at 490, 570, and 700 nm, respectively.

Our proposed RGB-achromatic aplanatic metalens not only focuses incoming light waves with normal incidence onto a single spot but also enable a much smaller and stronger spot size arising from corrected spherical aberration benefitting high-resolution images. To evaluate the degree of spherical aberration, a point source located at the optical axis is used to illuminate the RGB-achromatic aplanatic and nonaplanatic metalens in the simulation. The spherical aberration is defined as $\Delta s/s'$, where Δs represents the longitudinal FWHM of the point image.^[36] A smaller $\Delta s/s'$ indicates smaller spherical aberration, associated with better imaging quality. Our simulation results show that, for the RGB-achromatic aplanatic metalens, $\Delta s/s'$ is much smaller than that of RGB-achromatic nonaplanatic metalens for all three wavelengths (see Figure S5 in Note S3, Supporting Information). Four point sources located at the four corners of a $1 \mu\text{m} \times 1 \mu\text{m}$ square centered along the optical axis ($r = 0$) are considered as the object to be imaged. The RGB-achromatic aplanatic metalens show the best imaging performance, as the four associated image spots at all three wavelengths can be clearly distinguished (see Figure S6a–c in Note S3, Supporting Information). The image spots with the RGB-achromatic nonaplanatic metalens (Figure S6d–f, Supporting Information) and the chromatic nonaplanatic metalens (Figure S6g–i, Supporting Information) can

be distinguished only at 490 and 570 nm, respectively. For RGB-achromatic aplanatic metalenses with the same object distance but different image distances, the distance between the adjacent image points increases with the image distance (see Figure S7 in Note S3, Supporting Information). For different combinations of object and image distances, the image spots are always distinguishable, and the metalenses are always achromatic.

2.2. RGB-Achromatic Aplanatic Focusing and Imaging

An optical image of the fabricated metalens with NA = 0.635 is shown in Figure 2a, and a magnified scanning electron microscopy (SEM) image is shown in Figure 2b–c. Further details regarding the fabrication and optical measurements are provided in Note S4 (Supporting Information). The measured focal lengths are 365, 369, and 365 μm at 490, 570, and 700 nm, respectively, and undergo a rather low relative shift ($\approx 1\%$), indicating that the chromatic aberration at three RGB colors is well corrected (upper panels in Figure 3a,c,e). The metalens can also bring light at 530 and 630 nm to the brightest spots that have less than 10.7% focusing length deviation in comparison with those RGB wavelengths (upper panels in Figure 3b,d,f). The FWHM of the associated focal spots is slightly larger than the diffraction-limited spot size (lower panels of Figure 3a–e,g). This is mainly owing to the difference between the theoretical phase distributions extracted from Equation (1) (Figure S1, Supporting Information) and the phase distributions enabled by the metasurface units (Figure S2 a–c, Supporting Information). The extracted focusing efficiencies are 1.52%, 2.70%, and 6.54% at 490, 570, and 700 nm, respectively. The focusing efficiency can be enhanced by using low-loss dielectric materials, such as TiO_2 , as dielectric metasurfaces.

To reveal the practical use for optical imaging, we also fabricated an RGB-achromatic nonaplanatic metalens with the same NA and focal length as our RGB-achromatic aplanatic metalens, and compared their focusing and imaging performance. The measured focusing performance demonstrates the achromatic focusing effect because the focusing spots are all diffraction-limited under normal incidence (see Figure S10 in Note S5, Supporting Information). This RGB-achromatic nonaplanatic metalens has a focusing spot size comparable to that of the RGB-achromatic aplanatic metalens under normal incidence; however, the associated focusing effect deteriorates as the metalens is illuminated with a point source, corresponding to a broad incidence angle (see Figure S11 in Note S5, Supporting Information). For a practical image with a nonaplanatic metalens, the different rays scattered by the imaging targets do not converge into one focal point after the nonaplanatic metalens, deteriorating the image quality. Wide-spectrum white light from a lamp is filtered using bandpass filters to introduce RGB channels (centered at 490, 570, and 700 nm, with a bandwidth of $\approx 20 \text{ nm}$) to characterize the monochromatic imaging performance. First, the negative 1951 United States Air Force resolution test chart is used as the imaging target to evaluate imaging resolution. Figure 4a–f shows a comparison between the imaging results for the RGB-achromatic aplanatic and nonaplanatic metalenses, clearly indicating that the resolution of our aplanatic metalens is much better than that of the nonaplanatic metalens. This can be attributed to the fact that

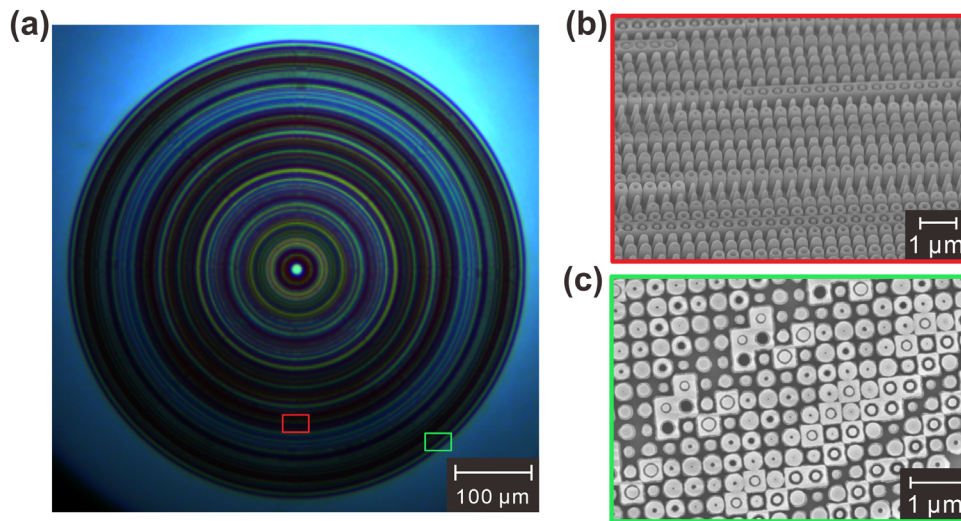


Figure 2. Photos of the fabricated RGB-achromatic aplanatic metalens with NA = 0.635. a) Optical image. b,c) Zoomed-in SEM images bounded by the red b) and green c) rectangles, respectively, in (a).

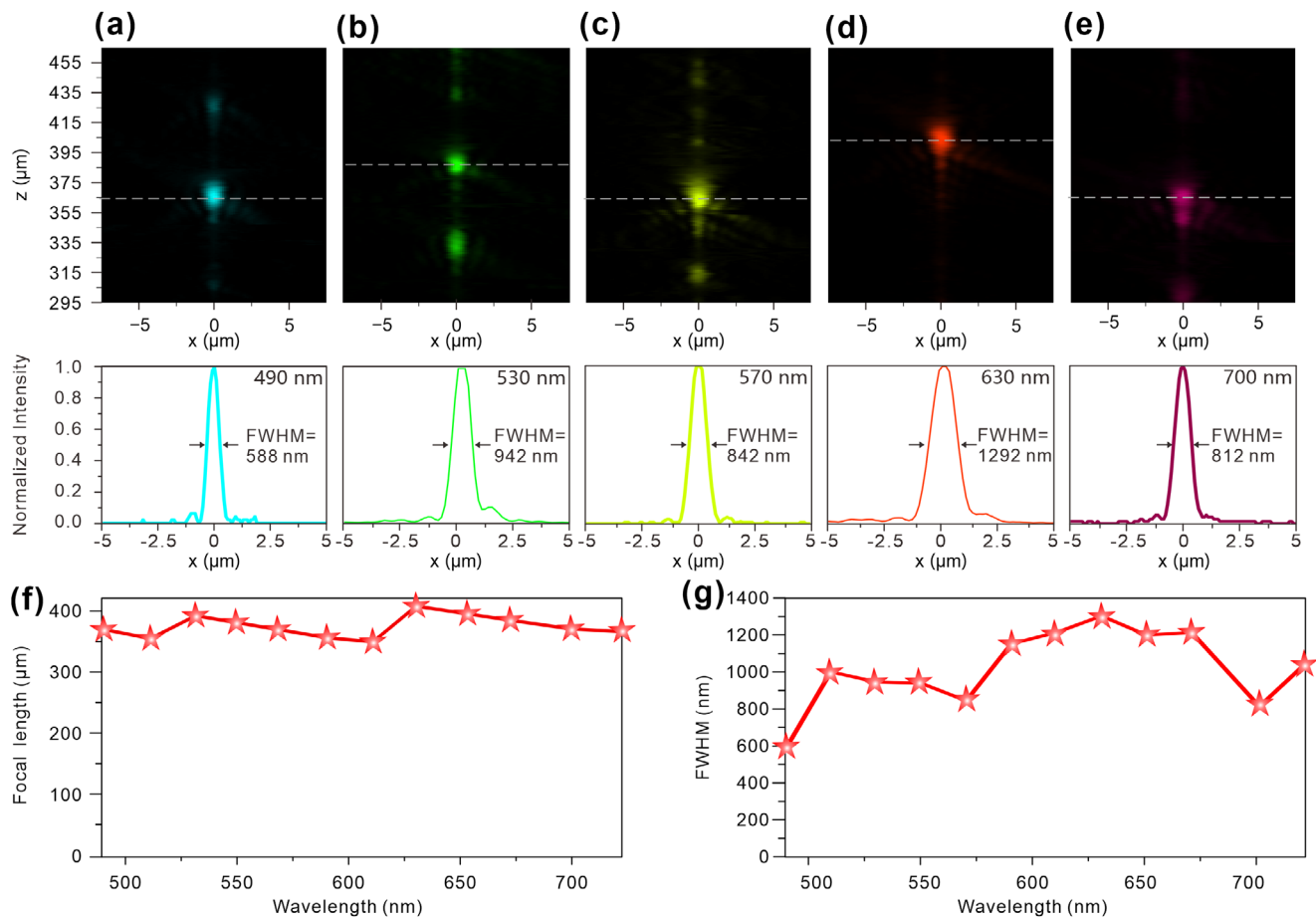


Figure 3. Measured focusing performance of the RGB-achromatic aplanatic metalens. a–e) Light intensity distributions in the x-z plane under a normal incidence at 490, 530, 570, 630, and 700 nm and their corresponding focusing intensity profiles along the dashed lines. f,g) Measured focal length f) and FWHM g) as a function of the incident wavelength.

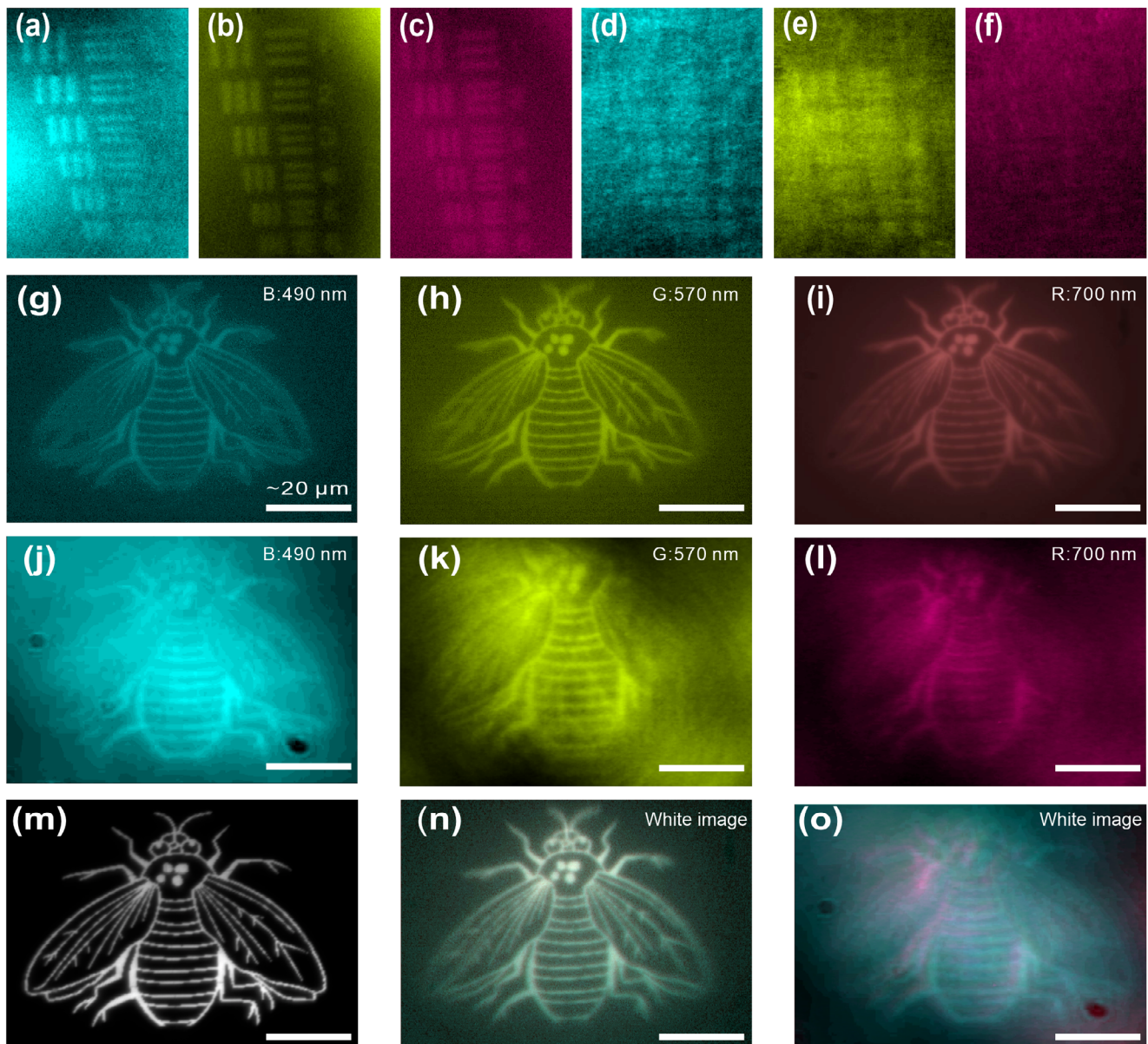


Figure 4. Imaging performance of the RGB-achromatic aplanatic and nonaplanatic metalens. a–f) Images of the seventh group in the negative 1951 United States Air Force resolution test chart with the RGB-achromatic aplanatic metalens a–c) and RGB-achromatic nonaplanatic metalens d–f) at 490, 570, and 700 nm, respectively. g–i) Images by the RGB-achromatic aplanatic metalens g–i) and RGB-achromatic nonaplanatic metalens j–l) with a bandpass filter centered at 490, 570, and 700 nm, respectively. m) Optical microscope image of the target object under wide-spectrum white light from a lamp. n,o) Captured image under white illumination with 25:2:5 RGB mixing ratio with the RGB-achromatic aplanatic metalens n) and RGB-achromatic nonaplanatic metalens o).

the aplanatic lens is able to focus the scattered light from the test chart, associated with a broad incidence angle, onto smaller focal spots owing to spherical aberration correction. Our metalens can even distinguish the narrowest line features on the chart, that is, $\approx 2.19 \mu\text{m}$ line width in element no. 6 from group no. 7, at all three RGB channels. In contrast, the images taken with the RGB-achromatic nonaplanatic metalens appear rather fuzzy in the same imaging region and, hence, a linewidth of $\approx 2.19 \mu\text{m}$ is indistinguishable. Our measurement shows that the imaging resolution for the nonaplanatic metalens is beyond $7.81 \mu\text{m}$ at

all three RGB channels, associated with the linewidth in element no. 1 from group no. 6.

A bee made of a thin Cr film using the laser direct writing method was used to demonstrate RGB imaging. A clear RGB image is obtained on the imaging plane using our RGB-achromatic aplanatic metalens (Figure 4g–i). In contrast, we obtain a much worse quality image with our nonaplanatic metalens due to the lack of spherical aberration correction (Figure 4j–l). The white image of our metalens, as shown in Figure 4n can well replicate the original optical microscopy image, as shown in Figure 4m,

which is attributed to excellent RGB-chromatic and spherical aberration correction. The image captured by the nonaplanatic metalens does not reproduce the original white image well due to the lack of spherical aberration correction (Figure 40). We have employed different exposure parameters of the CCD to extract the images for the RGB-achromatic aplanatic and nonaplanatic metalenses, resulting in different brightness for the images. Using our metalens, we can also implement practical color imaging for colorful slides under white-light illumination. The color slides, fabricated with color printing on highly transparent plastic boards, are illuminated without bandpass filters, as shown in Figure S9b (Supporting Information). The color slide comprises three primary colors (that is, RGB) and white. The color images are consistent with the original images (see Figure S12 in Note S5, Supporting Information). Notably, the slight color deviation mainly owing to the relatively low intensity of the blue channel. This can be further improved by adjusting the intensity ratios of the three RGB channels. A detailed summary of the optical imaging properties of the existing metalenses is provided in Table S1 in Note S5 (Supporting Information), which suggests no metalens has been reported with both high NA and correction of chromatic and spherical aberrations, highlighting the novelty of our findings. It is also worth emphasizing that, the NA of our RGB-achromatic aplanatic metalens is determined by the diameter and focal length, but it is not limited by the c-Si nanostructures and the design principle for correcting spherical aberrations. From the viewpoint of imaging quality, a better option is to enlarge the NA using a larger metalens, while keeping the focal length unchanged. However, fabricating larger metalens will increase the experimental difficulty and complexity of the electron beam lithography (EBL) process.

3. Conclusion

In summary, we have demonstrated an RGB-achromatic aplanatic metalens with high NA using c-Si nanostructures to introduce the required aplanatic phase profile. The focal length of our metalenses remains almost unchanged over a continuous wavelength region from 490 to 720 nm, while the associated focal spots are significantly smaller than those of RGB-achromatic metalens with spherical aberrations. The metalens can focus a continuous wavelength region from 490 to 720 nm into the same plane, whereas the associated focal spots are significantly smaller than those of RGB-achromatic metalens with spherical aberration. We demonstrated RGB-color imaging performance in transmission mode, with imaging resolution superior to that of a nonaplanatic metalens. Our results suggest a promising avenue for the design of metalens with a large NA while eliminating all optical aberrations. These RGB-achromatic aplanatic metalenses can be used in many relevant applications, such as high-resolution microscopic imaging, color imaging, and displays.

4. Experimental Section

Fabrication: The sample fabrication process of the metalens with $NA = 0.635$ starts with the deposition of silica film on an SOI wafer using inductively coupled plasma chemical vapor deposition (ICP-CVD), followed by spin-coating of the adhesive NOA61. Afterward, the SOI wafer with silica and NOA61, was bonded with a fused SiO₂ substrate. After ex-

posing with UV light for 4 h and baking at 50 °C for 3 days, the silicon substrate was removed with polishing and deep reactive ion etching (DRIE), the SiO₂ box layer is removed with HF acid, and the c-Si layer is reduced to 600 nm with ICP. Finally, the EBL process and ICP etching were used to obtain the patterned c-Si metalens (More fabrication details can be found in Figure S8 of Note S4, Supporting Information).

Measurements: Measurement setup for focusing (Figure S9a of Note S4, Supporting Information). The light from a tunable laser (NKT-SuperK EXTREME) was collected by O1 (objective 1, Sigmakoki EPL-5, 5×, $NA = 0.13$) and focused by the metalens. The light field was photographed by O2 (objective 2, Sigmakoki EPLE-50, 50×, $NA = 0.55$), TL (tube lens, Thorlabs, ITL200), and the CCD camera (Hamamatsu, C13440-20CU), all of which were mounted on the same displacement platform to scan different planes.

Measurement setup for resolution evaluation (Figure S9b of Note S4, Supporting Information). Wide-spectrum white light from a lamp (Thorlabs, SLS401) was filtered by a band-pass filter (Shenzhen NMOT, BP490/BP570/BP700, centered at 490, 570, and 700 nm, respectively, bandwidth of ≈ 20 nm) to characterize the monochromatic imaging performance. The incident light passed through a diffuser to reduce the speckles, and was then collected by O1 to illuminate the resolution chart (the negative 1951 United States Air Force resolution test chart). The image of the metalens was finally photographed by O2, TL, and the CCD camera (monochromatic imaging: Hamamatsu, C13440-20CU).

Measurement setup for imaging (Figure S9c of Note S4, Supporting Information). The incident light passed through a diffuser to reduce the speckles, and was then collected by O1 to illuminate the slide. For the measurement of color imaging, the filter was removed. The slide for monochromatic imaging was a bee made of a thin Cr film with the laser direct writing method, and the slide for color imaging was fabricated with color printing on highly transparent plastic boards. The image of the slide was zoomed by O3 (objective 3, Sigmakoki EPL-10, 10×, $NA = 0.3$) to work as the object, which was further imaged by the metalens. The image of the metalens was finally photographed by O2, TL, and the CCD camera (monochromatic imaging: Hamamatsu, C13440-20CU; color imaging: Thorlabs, DCU224C).

Supporting Information

Supporting Information is available from the Wiley Online Library or from the author.

Acknowledgements

This work is supported by National Natural Science Foundation of China (Grant No. 12074137), National Key Research and Development Project of China (Grant Nos. 2021YFB2801903, 2020YFA0710100). J.L, W.L, and H.X contributed equally to this work. The authors thank Dr. Guangwei Hu from Nanyang Technological University in Singapore for helpful discussions. The authors thank Wei Xu in the Center of Micro-Fabrication and Characterization (CMFC) of WNLO for the support in ICP etching, and the Center for Nanoscale Characterization & Devices (CNCD), WNLO, HUST for the support in SEM measurement. A.A. acknowledges support from the Air Force Office of Scientific Research and the Simons Foundation.

Conflict of Interest

The authors declare no conflict of interest.

Data Availability Statement

The data that support the findings of this study are available from the corresponding author upon reasonable request.

Keywords

achromatic, aplanatic, metalens

Received: August 2, 2023
Revised: February 13, 2024
Published online:

- [1] W. T. Chen, A. D. Y. Zhu, F. Capasso, *Nat. Rev. Mater.* **2020**, *5*, 604.
- [2] M. Khorasaninejad, A. Y. Zhuit, C. Roques-Carmes, W. T. Chen, J. Oh, I. Mishra, R. C. Devlin, F. Capasso, *Nano Lett.* **2016**, *16*, 7229.
- [3] M. Khorasaninejad, W. T. Chen, A. Y. Zhu, J. Oh, R. C. Devlin, D. Rousso, F. Capasso, *Nano Lett.* **2016**, *16*, 4595.
- [4] G. Zheng, H. Mühlenbernd, M. Kenney, G. Li, T. Zentgraf, S. Zhang, *Nat. Nanotechnol.* **2015**, *10*, 308.
- [5] L. L. Huang, H. Mühlenbernd, X. W. Li, X. Song, B. F. Bai, Y. T. Wang, T. Zentgraf, *Adv. Mater.* **2015**, *27*, 6444.
- [6] W. M. Ye, F. Zeuner, X. Li, B. Reineke, S. He, C. W. Qiu, J. Liu, Y. T. Wang, S. Zhang, T. Zentgraf, *Nat. Commun.* **2016**, *7*, 11930.
- [7] Z. Y. Yang, Z. K. Wang, Y. X. Wang, X. Feng, M. Zhao, Z. J. Wan, L. Q. Zhu, J. Liu, Y. Huang, J. S. Xia, M. Wegener, *Nat. Commun.* **2018**, *9*, 4607.
- [8] J. X. Wei, C. Xu, B. W. Dong, C. W. Qiu, C. K. Lee, *Nat. Photonics* **2021**, *15*, 614.
- [9] W. T. Chen, P. Török, M. R. Foreman, C. Y. Liao, W. Y. Tsai, P. R. Wu, D. P. Tsai, *Nanotechnology* **2016**, *27*, 224002.
- [10] M. B. Pu, X. Li, X. L. Ma, Y. Q. Wang, Z. Y. Zhao, C. T. Wang, C. G. Hu, P. Gao, C. Huang, H. R. Ren, X. P. Li, F. Qin, J. Yang, M. Gu, M. H. Hong, X. G. Luo, *Sci. Adv.* **2015**, *1*, e1500396.
- [11] A. Pors, M. G. Nielsen, S. I. Bozhevolnyi, *Optica* **2015**, *2*, 716.
- [12] A. Arbabi, E. Arbabi, Y. Horie, S. M. Kamali, A. Faraon, *Nat. Photonics* **2017**, *11*, 415.
- [13] J. X. Li, S. Kamin, G. X. Zheng, F. Neubrech, S. Zhang, N. Liu, *Sci. Adv.* **2018**, *4*, eaar6768.
- [14] Z. Huang, Y. Zheng, J. Li, Y. Cheng, J. Wang, Z.-K. Zhou, L. Chen, *Nano Lett.* **2023**, *23*, 10991.
- [15] M. Khorasaninejad, W. T. Chen, R. C. Devlin, J. Oh, A. Y. Zhu, F. Capasso, *Science* **2016**, *352*, 1190.
- [16] H. W. Liang, Q. L. Lin, X. S. Xie, Q. Sun, Y. Wang, L. D. Zhou, L. Liu, X. Y. Yu, J. Y. Zhou, T. F. Krauss, J. T. Li, *Nano Lett.* **2018**, *18*, 4460.
- [17] S. M. Wang, P. C. Wu, V. C. Su, Y. C. Lai, C. H. Chu, J. W. Chen, S. H. Lu, J. Chen, B. B. Xu, C. H. Kuan, T. Li, S. N. Zhu, D. P. Tsai, *Nat. Commun.* **2017**, *8*, 187.
- [18] S. Shrestha, A. C. Overvig, M. Lu, A. Stein, N. F. Yu, *Light Sci Appl* **2018**, *7*, 85.
- [19] Y. J. Wang, Q. M. Chen, W. H. Yang, Z. H. Ji, L. M. Jin, X. Ma, Q. H. Song, A. Boltasseva, J. C. Han, V. M. Shalaev, S. M. Xiao, *Nat. Commun.* **2021**, *12*, 5560.
- [20] W. T. Chen, A. Y. Zhu, V. Sanjeev, M. Khorasaninejad, Z. J. Shi, E. Lee, F. Capasso, *Nat. Nanotechnol.* **2018**, *13*, 220.
- [21] S. M. Wang, P. C. Wu, V. C. Su, Y. C. Lai, M. K. Chen, H. Y. Kuo, B. H. Chen, Y. H. Chen, T. T. Huang, J. H. Wang, R. M. Lin, C. H. Kuan, T. Li, Z. L. Wang, S. N. Zhu, D. P. Tsai, *Nat. Nanotechnol.* **2018**, *13*, 227.
- [22] Y. Zhou, I. I. Kravchenko, H. Wang, J. R. Nolen, G. Gu, J. Valentine, *Nano Lett.* **2018**, *18*, 7529.
- [23] Z. Y. Li, P. Lin, Y. W. Huang, J. S. Park, W. T. Chen, Z. J. Shi, C. W. Qiu, J. X. Cheng, F. Capasso, *Sci. Adv.* **2021**, *7*, eabe4458.
- [24] F. Aieta, M. A. Kats, P. Genevet, F. Capasso, *Science* **2015**, *347*, 1342.
- [25] J. E. Fröch, L. Huang, Q. A. A. Tanguy, S. Colburn, A. Zhan, A. Ravagli, E. J. Seibel, K. F. Böhringer, A. Majumdar, *eLight* **2023**, *3*, 13.
- [26] E. Arbabi, J. Q. Li, R. J. Hutchins, S. M. Kamali, A. Arbabi, Y. Horie, P. Van Dorpe, V. Gradinaru, D. A. Wagenaar, A. Faraon, *Nano Lett.* **2018**, *18*, 4943.
- [27] W. T. Chen, A. Y. Zhu, M. Khorasaninejad, Z. J. Shi, V. Sanjeev, F. Capasso, *Nano Lett.* **2017**, *17*, 3188.
- [28] M. Jang, Y. Horie, A. Shibukawa, J. Brake, Y. Liu, S. M. Kamali, A. Arbabi, H. W. Ruan, A. Faraon, C. H. Yang, *Nat. Photonics* **2018**, *12*, 84.
- [29] T. Gissibl, S. Thiele, A. Herkommer, H. Giessen, *Nat. Photonics* **2016**, *10*, 554.
- [30] W. B. Feng, J. C. Zhang, Q. F. Wu, A. Martins, Q. Sun, Z. H. Liu, Y. Long, E. R. Martins, J. T. Li, H. W. Liang, *Nano Lett.* **2022**, *22*, 3969.
- [31] H. W. Liang, A. Martins, B. H. V. Borges, J. Y. Zhou, E. R. Martins, J. T. Li, T. F. Krauss, *Optica* **2019**, *6*, 1461.
- [32] Y. J. Bao, Y. Yu, H. F. Xu, C. Guo, J. T. Li, S. Sun, Z. K. Zhou, C. W. Qiu, X. H. Wang, *Light Sci Appl* **2019**, *8*, 95.
- [33] Z. P. Zhou, J. T. Li, R. B. Su, B. M. Yao, H. L. Fang, K. Z. Li, L. D. Zhou, J. Liu, D. Stellinga, C. P. Reardon, T. F. Krauss, X. H. Wang, *ACS Photonics* **2017**, *4*, 544.
- [34] D. Sell, J. J. Yang, S. Doshay, K. Zhang, J. A. Fan, *ACS Photonics* **2016**, *3*, 1919.
- [35] A. Arbabi, Y. Horie, A. J. Ball, M. Bagheri, A. Faraon, *Nat. Commun.* **2015**, *6*, 7069.
- [36] C. Chen, W. E. Song, J. W. Chen, J. H. Wang, Y. H. Chen, B. B. Xu, M. K. Chen, H. M. Li, B. Fang, J. Chen, H. Y. Kuo, S. M. Wang, D. P. Tsai, S. N. Zhu, T. Li, *Light Sci Appl* **2019**, *8*, 99.
- [37] E. D. Palik, *Handbook of Optical Constants of Solids*, Academic Press, San Diego, **1998**, Vol. 3.